J. Fluid Mech. (1998), *vol.* 364, *pp.* 1–29 Printed in the United Kingdom

Experimental study of the fine-scale structure of conserved scalar mixing in turbulent shear flows. Part 2. $Sc \approx 1$

By KENNETH A. BUCH AND WERNER J. A. DAHM

Department of Aerospace Engineering, The University of Michigan, Ann Arbor, M1 48109-2118, USA

(Received 19 November 1996 and in revised form 7 November 1997)

Results are presented from an experimental study into the fine-scale structure of generic, $Sc \approx 1$, dynamically passive, conserved scalar fields in turbulent shear flows. The investigation was based on highly resolved, two-dimensional imaging of laser Rayleigh scattering, with measurements obtained in the self-similar far field of an axisymmetric coflowing turbulent jet of propane issuing into air at local outer-scale Reynolds numbers $Re_\delta \equiv u\delta/\nu$ of 11000 and 14000. The resolution and signal quality of these measurements allowed direct differentiation of the scalar field data $\zeta(\boldsymbol{x}, t)$ to determine the instantaneous scalar energy dissipation rate field $(Re\,Sc)^{-1}\boldsymbol{\nabla}\zeta\cdot\boldsymbol{\nabla}\zeta(\boldsymbol{x}, t)$. Results show that, as for large-Sc scalars (Buch & Dahm 1996), the scalar dissipation rate field consists entirely of strained, laminar, sheet-like diffusion layers, despite the fact that at $Sc \approx 1$ the scale on which these layers are folded by vorticity gradients is comparable to the layer thickness. Good agreement is found between the measured internal structure of these layers and the self-similar local solution of the scalar transport equation for a spatially uniform but time-varying strain field. The self-similar distribution of dissipation layer thicknesses shows that the ratio of maximum to minimum thicknesses is only 3 at these conditions. The local dissipation layer thickness is related to the local outer scale as $\lambda_D/\delta \equiv \Lambda Re_\delta^{-3/4}\, Sc^{-1/2}$, with the average thickness found to be $\langle\Lambda\rangle = 11.2$, with both the largest and smallest layer thicknesses following Kolmogorov ($Re_\delta^{-3/4}$) scaling.

1. Introduction

Turbulent mixing between gaseous streams is one of the largest and most important technological applications of turbulent flows, especially in problems involving combustion of non-premixed or partially premixed reactant streams. The high rates of molecular mixing achievable in turbulent flows permits high combustion heat release rates to be achieved, with applications ranging from the development of advanced aeropropulsion systems to the improvement of industrial combustion processes. In many cases, a key interest is the reduction of potentially harmful trace chemical species emissions that result from the complex mixing and reaction processes in the underlying turbulent flow.

In the absence of significant differential diffusion effects, the conservation of atomic elements and enthalpy in such chemically reacting flows permits the evolution of a potentially very large set of chemically reacting species to be reduced to the mixing of conserved scalar mixture fraction fields $\zeta(\boldsymbol{x}, t)$. Since such processes typically involve gaseous species, the resulting conserved scalar quantities have mass diffusivities D

comparable to the momentum diffusivity ν in the underlying flow, and thus their Schmidt number $Sc \equiv \nu/D$ is typically unity. In many cases involving chemical reactions, it is physical processes occurring at the diffusive scales that can have a crucial effect on the outcome of the reactions, and thus an understanding of the fine-scale structure of $Sc \approx 1$ conserved scalar mixing in turbulent shear flows is essential for modelling the coupling between molecular mixing and chemical reactions in turbulent combustion problems. It is well established that the fine-scale structure of the conserved scalar mixing process is intimately connected with the detailed non-equilibrium chemical kinetics responsible for the formation of trace pollutant emissions such as nitrogen oxides and volatile organic compounds. Virtually all modern theories of non-equilibrium mixing-chemistry coupling in turbulent flows are based on assumptions about the fine-scale structure of $Sc \approx 1$ conserved scalar fields.

The present study thus aims to identify the physical characteristics of the fine structure of $Sc \approx 1$ scalar fields. In a previous companion paper (Dahm & Buch 1996, hereinafter referred to as Part 1) we examined the fine-scale structure associated with the mixing of Sc 1 conserved scalar fields in turbulent shear flows. In a future companion paper (Part 3) we shall examine the implications of this fine-scale structure for non-equilibrium mixing-chemistry coupling in turbulent reacting flows.

1.1. *Background*

The basic concepts essential to the formulation adopted here for assessing the fine-scale structure of conserved scalar mixing in turbulent flows can be found in §2 of Part 1. A major result of Part 1 was the observation that, for Sc 1 scalars in turbulent flows, essentially all the scalar energy dissipation rate field $\chi(\boldsymbol{x}, t) \equiv (Re\, Sc)^{-1} \boldsymbol{\nabla}\zeta \cdot \boldsymbol{\nabla}\zeta(\boldsymbol{x}, t)$ is concentrated entirely in thin, laminar diffusion layers. These layers result from the local competing effects of the principal compressive strain rate induced by the underlying flow, which acts to reduce the gradient lengthscale, and molecular diffusion of the scalar which acts to broaden the gradient scale. As was detailed in §7 of Part 1, the structure of this local strain field can be reduced to a single parameter $\sigma(t)$. The scalar transport equation precludes line-like ($\sigma < 0$) fine-scale structures in the scalar field but permits sheet-like ($\sigma > 0$) structures between local scalar endpoint values ζ^+ and ζ^- (see figure 25 of Part 1). In contrast, the stretching term in the vorticity transport equation allows both line-like and sheet-like structures to be indefinitely sustained. The vorticity field thus shows the complexity of line-like, sheet-like, and more intricate intermediate fine-structure topologies from which turbulence gains its notoriety, while the inner scale structure of Sc 1 conserved scalar fields is restricted to the single, comparatively simple, locally sheet-like topology, and might thus be more amenable to modelling. Fully resolved two- and three-dimensional experimental data for Sc 1 scalar fields in Part 1 showed good agreement with this locally sheet-like fine-scale structure (e.g. figures 7–13 of Part 1), and good agreement with the local canonical solution for the internal structure of this sheet-like topology (e.g. figures 28–31 of Part 1).

The arguments for a locally time-varying but spatially uniform strain field that leads to formation and maintenance of this purely sheet-like fine structure in the scalar field are well justified for Sc 1 scalars by the resulting disparity in gradient lengthscales in the vorticity and scalar fields. The competing effects of the most compressive local principal strain rate $\epsilon(t)$ and molecular diffusion with mass diffusivity D (see (7.6) of Part 1) establish an equilibrium strain-limited scalar diffusion thickness $\lambda_D \sim (D/\epsilon)^{1/2}$, closely related to the Batchelor scale. A similar competition between the effects of strain and diffusion of vorticity establishes a local strain-limited vorticity thickness $\lambda_\nu \sim (\nu/\epsilon)^{1/2}$, closely related to the Kolmogorov scale and giving the smallest scale on

which velocity gradients can be sustained. The ratio of the scalar and vorticity diffusivities establishes the ratio between these two scales as $\lambda_D/\lambda_\nu \approx Sc^{-1/2}$, where $Sc \equiv (\nu/D)$. Thus when $Sc \gg 1$, the resulting $\lambda_\nu \gg \lambda_D$ and the notion of a spatially uniform strain field over lengthscales significantly larger than λ_D is easily satisfied.

Such a comparison of the local gradient scales λ_D and λ_ν offers a useful perspective for understanding potential differences between the fine structure of $Sc \gg 1$ and $Sc \approx 1$ conserved scalar fields in turbulent flows. In particular, while for $Sc \gg 1$ there is a wide disparity in the gradient lengthscales, with $\lambda_D \ll \lambda_\nu$ as noted above, for $Sc \approx 1$ these two lengthscales are essentially the same. This has two important consequences for the fine structure of $Sc \approx 1$ scalar fields. First, in a Lagrangian frame moving with any point in the flow, the validity of a linear representation of the local flow field over regions of the order of λ_D is clearly justified for $Sc \gg 1$, but would at best be marginally valid for $Sc \approx 1$. To the extent that this linearized picture of the local flow field plays a key role in establishing the diffusion layer structure seen for $Sc \gg 1$ in Part 1, it is questionable if such a comparatively simple fine-scale structure can be expected at $Sc \approx 1$. Secondly, even if the marginal validity of this linear representation of the flow did allow such strained diffusion layers of thickness λ_D to form, it is insightful to view the effect of Sc on the subsequent evolution of such layers in terms of the relative scales of stretching (due to the strain field) and folding (due to the vorticity field) of the layer. For $Sc \gg 1$ the smallest scale λ_ν on which folding of the layer can occur is still of order $Sc^{1/2}$ larger than the layer thickness λ_D. As a result, within a region extending a few λ_D in any direction, the diffusion layer would undergo stretching but virtually no folding, since the scale λ_ν of the local vorticity gradient requires regions of this size to be in essentially solid body rotation. For $Sc \approx 1$, on the other hand, the local scale λ_ν of the strain rate and vorticity gradients is essentially the same as the layer thickness λ_D, and thus within such a region the layer would undergo not only stretching, but also folding back onto itself. This suggests that the fine-structure topology might not remain layer-like, and instead might take an entirely different form.

1.2. *The present study*

Here we report results from an experimental investigation of the fine-scale structure associated with molecular mixing of $Sc \approx 1$ conserved scalar fields in turbulent shear flows. As was the case in Part 1, we will be concerned solely with the mixing of dynamically passive scalars, for which the underlying velocity field $\boldsymbol{u}(\boldsymbol{x}, t)$ is not directly affected by the conserved scalar field $\zeta(\boldsymbol{x}, t)$. Moreover, as was also the case in Part 1, we will restrict our present attention to the mixing process in incompressible turbulent shear flows, though we believe that many of these results carry over to compressible turbulent flows as well. Finally, we will address only the molecular diffusion due to gradients in the scalar concentration field, and will not address additional diffusion due to thermophoretic or other effects which may be relevant in some problems.

In view of the arguments above regarding potential differences between $Sc \gg 1$ and $Sc \approx 1$ mixing, our principal objective is to answer two questions. First, is there any coherent underlying fine structure associated with $Sc \approx 1$ mixing of conserved scalars at the small scales of turbulent flows? In particular, does the sheet-like fine structure seen for $Sc \gg 1$ in Part 1 extend to $Sc \approx 1$ scalar fields, despite the arguments above regarding the different lengthscales involved in the underlying stretching and folding process? Secondly, if a coherent fine-scale structure is present even at $Sc \approx 1$, what are its characteristics and in what ways does it differ from the thin, strained, locally one-dimensional laminar diffusion layers seen in Part 1 for $Sc \gg 1$?

The present study is based on highly resolved two-dimensional imaging of laser Rayleigh scattering from the generic $Sc \approx 1$ conserved scalar field that results from mixing between gaseous propane and air in a turbulent shear flow. As was the case in Part 1, the measurements are obtained in the self-similar far field of an axisymmetric coflowing turbulent jet. However, in Part 1 the scalar field measurements extended over spatial regions that were of the order of the local inner scale λ_ν and much smaller than the local outer scale δ, and consequently the arguments presented there for quasi-universality of the fine structure on the scale λ_ν were readily satisfied. Furthermore, the notion of isotropy on these scales was readily justifiable, so that statistics obtained from two-dimensional measurements could be converted to the corresponding three-dimensional gradient statistics. In the present study the measurements extend over spatial regions that are of the order of the outer scale δ and many times larger than the inner scale λ_ν, so that both these arguments are more difficult to justify. Regarding the former, this merely means that the fine-scale structure seen over lengthscales of the order of λ_ν should still be universal, but the small-scale structure (i.e. the patterns into which this fine-scale structure is arranged by the continual stretching and folding of the underlying flow field on lengthscales between the inner scale λ_ν and the outer scale δ) will depend at least to some extent on the local outer-scale Reynolds number Re_δ and on the particular shear flow at hand. For the latter, the departures from isotropy will be seen to be small enough for such corrections to still be reasonable. Consequently, the fine-scale structure and its associated statistics obtained from these measurements are believed to be largely representative of the quasi-universal structure that results from the mixing of $Sc \approx 1$ conserved scalars in all turbulent shear flows.

The presentation is organized as follows. In §2, we give a brief overview of the planar laser Rayleigh imaging technique used to obtain very highly resolved measurements of the $Sc \approx 1$ conserved scalar field in a turbulent shear flow. Sample results of the local conserved scalar and scalar dissipation fields are presented in §3, where we identify the underlying structural elements of the scalar mixing process. Section 4 presents various statistics associated with this fine structure, §5 examines the internal structure of the scalar dissipation field and makes comparisons with the analytical solutions of Part 1, and in §6 the distribution of dissipation layer thickness is determined. Section 7 considers the scaling of the dissipation layer thicknesses, and in §8 we summarize conclusions from this study and discuss their implications for mixing and chemical reactions in turbulent flows.

2. Experimental technique and resolution

These experiments were based on high-resolution two-dimensional imaging of laser Rayleigh scattering in the self-similar far field of an axisymmetric coflowing turbulent jet in air. The measurements were conducted in the Turbulent Diffusion Flame (TDF) tunnel at the Combustion Research Facility (CRF) of Sandia National Laboratories. The jet was established in the $30\text{ cm} \times 30\text{ cm} \times 200\text{ cm}$ test section of a forced-draft vertical wind tunnel with a free-stream velocity U_∞ by issuing a jet of undiluted technical grade propane with momentum flux J_0 through a 7.7 mm diameter straight cylindrical tube, which originated in the settling section of the tunnel and entered the test section through a 9:1 area contraction. Both the free-stream velocity in the tunnel and the jet momentum flux were determined from mass flow meter measurements. The beam from a 300 mJ/pulse Nd:YAG laser was frequency doubled to 532 nm and optically arranged to form a thin, fixed vertical light sheet passing radially through the flow and containing the jet centreline. Propane was selected for the jet fluid since it has

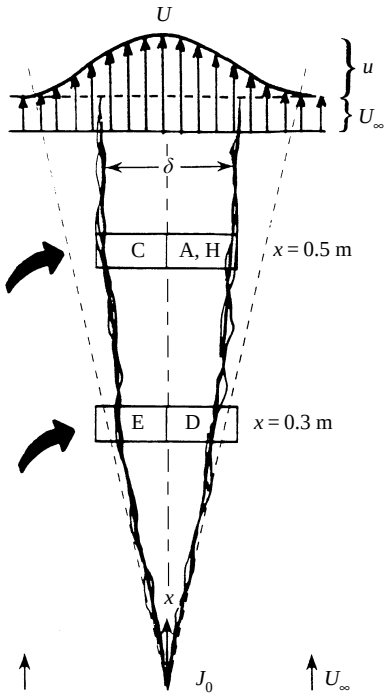

FIGURE 1. Schematic showing relative size and location of the imaging area for each case. Letters identify case designations in tables 1 and 2.

Designation	J_0 (N)	U_∞ (m s^{-1})	x (m)	x/ϑ_1	$Re_\delta \equiv u\delta/\nu$
A0689	0.041	15.0	0.5	75	11000
C0689	0.041	15.0	0.5	75	11000
D0689	0.041	15.0	0.3	45	14000
E0689	0.041	15.0	0.3	45	14000
H0689	0.041	15.0	0.5	75	11000

TABLE 1. Experimental conditions.

a Rayleigh scattering cross-section approximately thirteen times that of the ambient air in the tunnel. This relatively large cross-section difference allows accurate measurements of the propane mole fraction field within the plane of the laser sheet via planar Rayleigh imaging from the flow.

The resulting propane mass fraction field corresponds to a generic $Sc \approx 1$ conserved scalar field $\zeta(\boldsymbol{x}, t)$, and thus allows study of the fine-scale structure that results from the turbulent mixing of any such near-unity Sc scalar field. It should be noted that the interest here is not restricted to the mixing of propane and air, instead these two constituents are employed merely to permit access to the generic fine structure of $Sc \approx 1$ conserved scalar fields in turbulent shear flows.

2.1. *Flow conditions*

Measurements were obtained for $J_0 = 0.041$ N and $U_\infty = 15.0$ m s^{-1} at four different locations in the self-similar far field of the turbulent shear flow, as indicated schematically in figure 1. The prefixes of the five cases listed in table 1 correspond to

these measurement locations. These include two axial locations at downstream distances $x = 0.3$ m and 0.5 m from the jet source, which in relation to the nozzle diameter d_0 correspond to $x/d_0 = 39$ and 65. In terms of the proper downstream similarity coordinate for axisymmetric coflowing turbulent jets, these two axial locations correspond to $x/\vartheta = 45$ and 75, placing the measurements well into the self-similar far field of the flow and between the jet-like ($x/\vartheta \to 0$) and wake-like ($x/\vartheta \to \infty$) similarity scaling limits (see §4.3 of Part 1). The corresponding local outer-scale Reynolds numbers $Re_\delta \equiv u\delta/\nu$ at these two axial locations are 14000 and 11000 respectively, where the notation is the same as in Part 1.

The experiments were designed so that buoyancy effects were negligible at the conditions listed in table 1. This is quantified in terms of the proper buoyancy (Morton) lengthscale l_M for turbulent jets issuing with combined momentum and buoyancy flux from a jet source, which scales their transition from the momentum-dominated to the buoyancy-dominated regimes (e.g. Papanicolaou & List 1988). The pure jet-like (buoyancy-free) limit of the flow holds for $x/l_M < 1$, with buoyancy and initial momentum effects both important over $1 < x/l_M < 10$, and with the flow essentially reaching the pure plume-like (buoyancy-driven) limit beyond $x/l_M > 10$. For the two downstream locations in table 1, the corresponding values of x/l_M are 0.27 and 0.45, and are thus both well within the non-buoyant regime.

For each case in table 1, typically 100 individual, temporally uncorrelated, spatially resolved data planes were collected, each consisting of 256×512 individual point measurements of the conserved scalar field $\zeta(\boldsymbol{x}, t)$. Of these typically 50 to 75 planes were identified as being essentially dust-free for detailed analyses of the fine structure associated with the $Sc \approx 1$ conserved scalar mixing process.

2.2. *Spatial and temporal resolution*

The laser sheet had a pulse duration of typically 10 ns, and its 1/e thickness was measured as 230 μm and varied insignificantly over the imaged portion of the sheet. Rayleigh scattered light from the propane and air in the imaged portion of the laser sheet was measured with a 12-bit slow-scanned thermoelectrically cooled imaging array. To avoid degrading the spatial resolution, no image intensification was used. The array was sampled to produce individual data planes of the Rayleigh signal in a 256×512 element format, with each element having dimensions 23 μm × 23 μm, and the light collection optics were arranged to produce a 1:1 image ratio. The resulting volume in the flow imaged into each pixel in the array had characteristic spatial dimensions of 23 μm × 23 μm × 230 μm, and its output represents the Rayleigh signal integrated over the 10 ns laser pulse duration. This image volume and integration time must be compared with the finest spatial and temporal scales of the local conserved scalar field.

The procedure for estimating the smallest length and time scales appearing in the scalar field for these $Sc \approx 1$ experiments is identical to that outlined in §4.3 of Part 1; only the Schmidt number is different. In this case, as indicated in table 2, the 10 ns laser pulse duration was fast enough that the temporal resolution requirement $\Delta t \quad \lambda_D/U$ could be easily satisfied (though the elapsed time ΔT between acquisition of successive data planes was very large in comparison with λ_D/U, so that the planes were all temporally uncorrelated). Maps similar to those in figure 5 of Part 1 for the spatial resolution requirements can be constructed for each of the two axial locations in the present experiments. The resulting spatial resolution achieved for all five cases in table 1 are shown in table 2, where it can be noted that all the measurements are fully

Designation	λ_D (μm)	$\Delta x, \Delta y$ (μm)	Δz (μm)	λ_D/U (ms)	Δt (ms)
A0689	1060	23	230	0.060	10^{-5}
C0689	1060	23	230	0.060	10^{-5}
D0689	690	23	230	0.036	10^{-5}
E0689	690	23	230	0.036	10^{-5}
H0689	1060	23	230	0.060	10^{-5}

TABLE 2. Spatial and temporal resolution estimates.

resolved, since max $(\Delta x, \Delta y, \Delta z) < \frac{1}{2}\lambda_D$. Evidence will be seen in the results that follow that this resolution is indeed sufficient to resolve the fine-scale structure of the conserved scalar field in these experiments.

2.3. *Data reduction*

The Rayleigh scattered light intensity collected by the array was converted to the conserved scalar (propane mass fraction) field $\zeta(\boldsymbol{x}, t)$ following a procedure similar to that in §4.5 of Part 1. The fixed pattern in the array was first determined from dark measurements and subtracted from each data plane. Next the transfer function obtained from measurements with pure air in the test section was used to correct for flat field effects and other non-idealities in the optical system. The pure-air signal level was then subtracted, the resulting data converted from propane mole fraction to mass fraction, and finally rescaled to 8-bits digital depth. Lastly, a uniform 5×5 pixel filter was applied over each data plane, which is large enough to remove most shot noise effects prior to differentiation yet small enough relative to λ_D so as not to significantly affect the spatial resolution of the measurements (see table 2). The resulting conserved scalar data $\zeta(\boldsymbol{x}, t)$ were then used to generate the two-dimensional scalar dissipation fields $\chi(\boldsymbol{x}, t)$ via the template in (4.9) of Part 1, and to generate the in-plane scalar gradient vector orientations $\tan \vartheta(\boldsymbol{x}, t)$ via the template in (4.10) of Part 1.

2.4. *Noise analysis*

Whereas the uncooled photodiode array in Part 1 operated in the camera noise limited regime, for which the noise level σ_ζ in the data is independent of the signal, the 12-bit thermoelectrically cooled and slow-scanned CCD array used in the present measurements has a much lower relative camera noise level, and consequently operates in the shot noise limited regime. Thus the noise level σ_ζ in these data scales with the square root of the signal, and the signal-to-noise level increases with the square root of the signal. Measurements of the remaining shot noise level in the $\zeta(\boldsymbol{x}, t)$ data from §2.3 above showed that σ_ζ was less than 1 digital signal level in the pure air data, whereas the highest conserved scalar signal levels spanned the full 256 digital signal levels attainable with 8-bit data. Scaling this noise level with the square root of the Rayleigh signal level derived from the air and propane scattering cross-sections and the local propane mole fraction indicates a noise level σ_ζ of about 2 digital signal levels out of the 100 digital signal levels corresponding to the mean scalar value. The corresponding noise in the scalar dissipation fields that result from differentiation of these data can be obtained as outlined in Appendix A of Part 1, with the resulting levels being approximately 1 digital level out of 25 at the mean scalar dissipation value, and 2.2 out of 256 at the peak dissipation value. No explicit smoothing or filtering has been applied to any of these dissipation fields.

3. Structure of the scalar and dissipation rate fields

Typical results are presented in this section for the $Sc \approx 1$ conserved scalar fields $\zeta(\boldsymbol{x}, t)$ and the scalar energy dissipation rate fields $\chi(\boldsymbol{x}, t) \equiv (Re\,Sc)^{-1}\,\boldsymbol{\nabla}\zeta\cdot\boldsymbol{\nabla}\zeta(\boldsymbol{x}, t)$ obtained at each of the four locations in figure 1.

3.1. *Sample fields*

Figures 2–5 show typical data planes for each of the measurement conditions listed in tables 1 and 2. In each case, the jet centreline coincides with either the right- or left-hand edge of each data plane, as indicated by the axes, which also give the spatial extent of each plane in terms of the local strain-limited vorticity diffusion lengthscale λ_ν. Since the flow and imaging conditions for all these cases were identical except for the two differing downstream locations, the relative size of these planes depends only on the downstream location. Note also that, unlike the Sc 1 measurements in Part 1, in these $Sc \approx 1$ measurements the field of view is not confined to the inner flow scale λ_ν, but spans from the jet centreline to slightly beyond the outer edge of the flow. As a consequence, it must be kept in mind that assumptions regarding isotropy of the scalar gradient field invoked in deconvolving certain statistical measures of the dissipation field are likely to be poorer approximations than was the case for the Sc 1 measurements in Part 1. This will be examined in more detail in the sections that follow.

For the conserved scalar fields $\zeta(\boldsymbol{x}, \mathrm{t})$ in part (*a*) of each figure, the 256 different colour levels discernible with these 8-bit data each denote narrow ranges of the local instantaneous conserved scalar value. In each case, pure blue denotes the lowest range of scalar values, beginning at $\zeta = 0$ (pure ambient fluid), with colours ranging from blue to red identifying linearly increasing scalar values, and with pure red denoting the highest 0.1 % of values seen. Similarly, for the scalar dissipation rate fields $\chi(\boldsymbol{x}, t)$, pure black denotes the lowest range of dissipation values, beginning at $\chi = 0$, with the remaining 255 colours ranging from pure blue to pure red denoting linearly increasing dissipation rates. The highest 0.1 % of the dissipation rates are again typically mapped to pure red. In the logarithmic presentations $\log_e \chi(\boldsymbol{x}, t)$, the lowest level is again coloured black and denotes zero and very low dissipation rates, with the remaining colours identifying logarithmically increasing dissipation rates, and with pure red again typically denoting the highest 0.1 % of the logarithmic dissipation rate values.

The derivatives computed within each spatial data plane give the projection of the true three-dimensional scalar gradient vector field $\boldsymbol{\nabla}\zeta(\boldsymbol{x}, t)$ onto the data plane. Note that the dissipation values shown thus underestimate the true dissipation wherever the scalar gradient vector has a strong out-of-plane component. However it should be noted that while the dissipation fields obtained may underestimate the *magnitude* of the true dissipation values, they nevertheless provide an accurate picture of the *structure* of the dissipation field, except at those points where the true scalar gradient vector points virtually perpendicularly to the imaging plane. Furthermore, subject to the limitations on the assumption of isotropy in the scalar gradient vector field, even statistical quantities associated with the magnitude of the true dissipation rate field can be correctly obtained from the present two-dimensional approximations using the techniques described in Dahm & Buch (1989) and in the Appendix.

3.2. *Structure*

The scalar dissipation rate fields in figures 2–5 allow the basic structural features associated with mixing of $Sc \approx 1$ conserved scalars in turbulent flows to be identified.

As can be seen in the linear dissipation maps in these figures, and even more clearly in the logarithmic presentations (which reveal the structure at low dissipation values), the scalar dissipation rate field is largely concentrated in a set of convoluted sheet-like strained laminar diffusion layers. That the canonical structure seen is due to the intersection of a sheet-like topology with the measurement plane can be deduced from the observation that, if line-like or similar topologies were present, then roughly circular intersections should be seen wherever the measurement plane coincides at least approximately with the diametral plane of such a structure. Such circular intersections would then occur with a probability consistent with the near-isotropic scalar gradient vector orientations, yet essentially no such topologies can be found in the data.

The characterization of the fine-scale structure in the present $Sc \approx 1$ dissipation fields as locally sheet-like appears appropriate, since the radius of curvature of these layers is typically somewhat larger than their thickness. However the layers clearly are much more contorted than was the case at Sc 1, and in some places the local radius of curvature is even comparable to the local layer thickness. Note also that, as was the case for Sc 1 in Part 1, both isolated and interacting layers can be identified. Consistent with this, note that there are no layers at this location in the flow bounded by scalar endpoint values $(\zeta^+, \zeta^-) = (1, 0)$, and very few layers have $\zeta^- = 0$. Essentially all the dissipation layers are between two different mixed fluid states, consistent with the results for Sc 1 in Part 1.

Although the basic fine-structure element in both the Sc 1 and the $Sc \approx 1$ scalar dissipation fields appears to be a set of sheet-like layer structures, there are two major differences due to the different Schmidt numbers. The layers in the Sc 1 fields are locally parallel to neighbouring layers, and are distorted by the underlying flow over a lengthscale that is typically many times greater than the thickness λ_D of the layers. By comparison, individual layers in the $Sc \approx 1$ fields are generally oriented very differently from adjacent layers, and the scale over which they are distorted is typically at most a few layer thicknesses. As discussed in §1.1, the two relevant lengthscales associated with this stretching and folding of the dissipation layers are the local strain-limited vorticity diffusion scale λ_ν and the corresponding local strain-limited scalar diffusion scale λ_D, related as $\lambda_D = \lambda_\nu Sc^{-1/2}$. For the results in Part 1, where $Sc \approx 2000$, this gives $\lambda_D/\lambda_\nu \approx 1/45$, so the scalar field varied on a much finer scale than that on which gradients in the underlying vorticity and strain rate fields occurred. As a consequence, over distances many times the characteristic thickness λ_D of the dissipation layers, the vorticity and strain rate fields were essentially uniform. Thus any given layer maintained essentially the same thickness and orientation over a lengthscale many times its own thickness. Moreover, neighbouring layers were subjected to the same vorticity and strain rate values, and therefore had similar orientations and thicknesses.

On the other hand, when the Schmidt number is near unity, the two lengthscales λ_D and λ_ν are essentially the same, and consequently the vorticity and strain rate remain uniform only over a lengthscale typically comparable to the local thickness λ_D of the dissipation layer. Any given layer therefore maintains its orientation over an extent comparable to at most a few times its local thicknesses before differential rotation effects due to gradients in the vorticity field distort or even fold the layer back onto itself. This can be seen in the $Sc \approx 1$ results in figures 2–5. Furthermore, neighbouring layers are subjected to significantly different vorticity and strain rate values, and therefore can have very different orientations and somewhat different thicknesses. The results in figures 2–5 confirm that this is the case. Moreover, keeping in mind that neighbouring layers in the $Sc \approx 1$ scalar dissipation fields will generally not remain

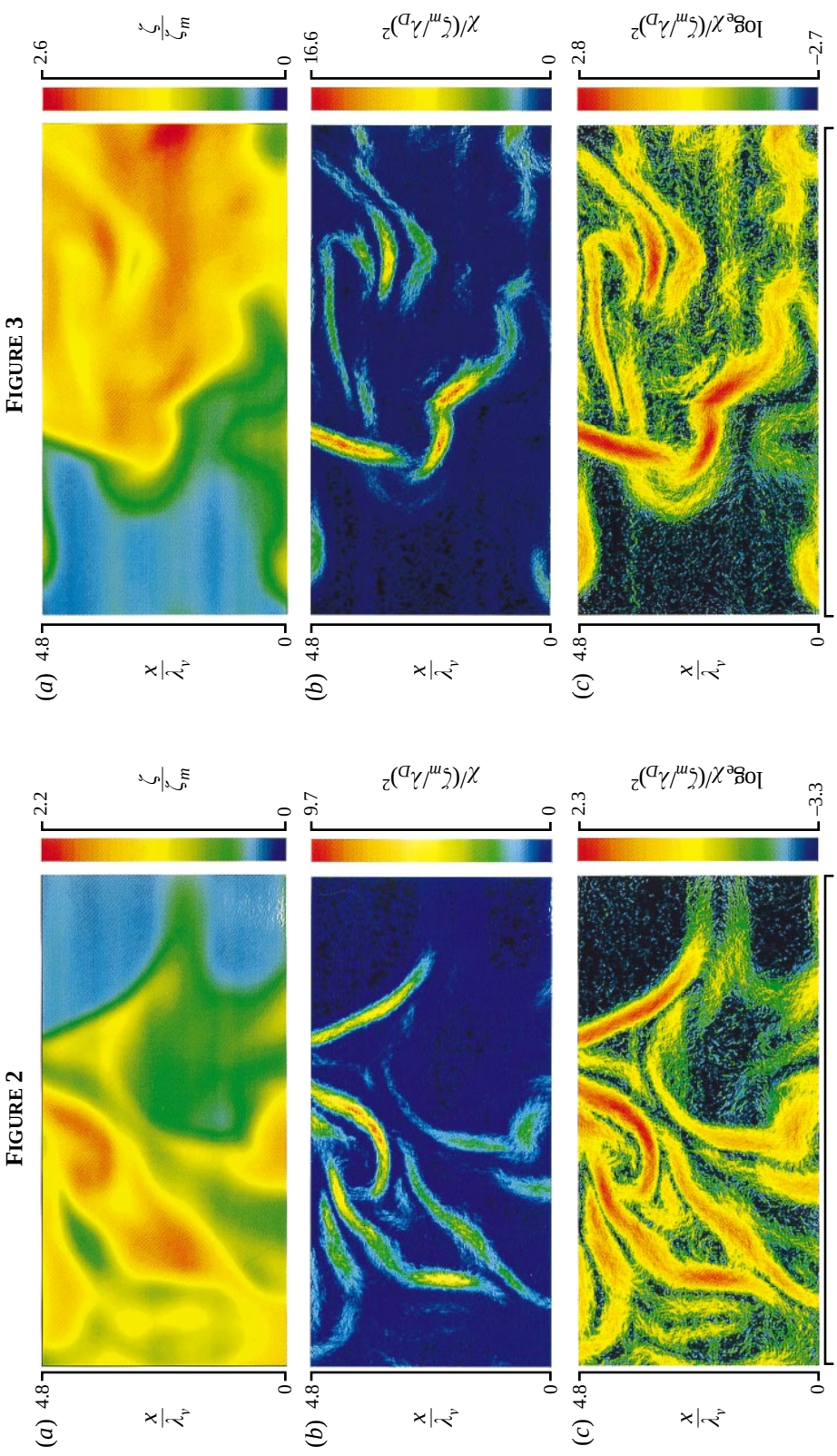

FIGURE 2. Typical data planes from data set H0698 showing the instantaneous (*a*) conserved scalar field, $\zeta(\boldsymbol{x}, t)$; (*b*) scalar dissipation field, $\chi(\boldsymbol{x}, t) = \boldsymbol{\nabla}\zeta \cdot \boldsymbol{\nabla}\zeta(\boldsymbol{x}, t)$; and (*c*) logarithm of the scalar dissipation field, $\log_e \chi(\boldsymbol{x}, t)$.

FIGURE 3. Typical data planes from data set C0689 showing (*a*) $\zeta(\boldsymbol{x}, t)$, (*b*) $\chi(\boldsymbol{x}, t) = \boldsymbol{\nabla}\zeta \cdot \boldsymbol{\nabla}\zeta(\boldsymbol{x}, t)$, and (*c*) $\log_e \chi(\boldsymbol{x}, t)$.

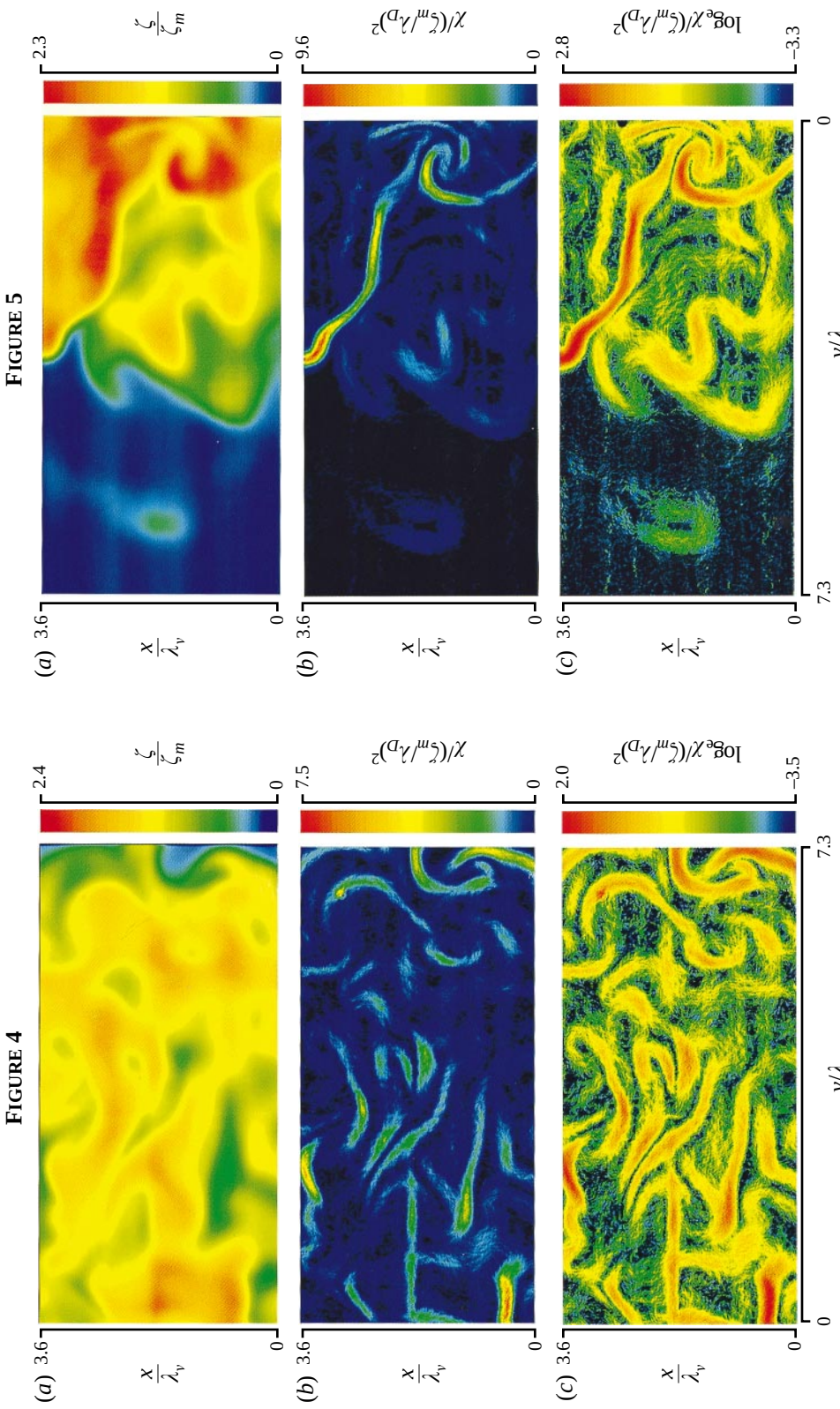

FIGURE 4. Typical data planes from data set D0698 showing (*a*) $\zeta(\boldsymbol{x}, t)$, (*b*) $\chi(\boldsymbol{x}, t) = \boldsymbol{\nabla}\zeta \cdot \boldsymbol{\nabla}\zeta(\boldsymbol{x}, t)$, and (*c*) $\log_e \chi(\boldsymbol{x}, t)$.

FIGURE 5. Typical data planes from data set E0689 showing (*a*) $\zeta(\boldsymbol{x}, t)$, (*b*) $\chi(\boldsymbol{x}, t) = \boldsymbol{\nabla}\zeta \cdot \boldsymbol{\nabla}\zeta(\boldsymbol{x}, t)$, and (*c*) $\log_e \chi(\boldsymbol{x}, t)$.

parallel, it appears that even the low- to mid-ranged scalar dissipation rates (blue to green colour values in the logarithmic maps in figures 2–5) also correspond to layer-like structures, but that these are locally oriented strongly tangent to the measurement plane and thus appear at lower values in these two-dimensional gradient approximations.

3.3. *Magnitudes*

As was the case in the $Sc \gg 1$ results from Part 1, the scalar dissipation fields in the linear maps in figures 2–5 show that high dissipation values occur only rarely and are clearly confined to easily identifiable layer-like structures. Low dissipation values, corresponding to blue colours in these same linear dissipation maps, cover a much larger volume fraction of the flow. An assessment of the distribution of scalar dissipation rates, including an isotropy correction to account for the missing gradient vector component, is given in §4.2. Note that, while the linear dissipation maps give a clear view of the internal intermittency, they do not allow as clear an identification of their underlying topology at low dissipation rates. By comparison, the corresponding logarithmic colour maps, especially when coupled with the arguments regarding layer orientations noted above, clearly reveal the structure at low values, and suggest that even these low dissipation rates are also concentrated in laminar sheet-like diffusion layers.

3.4. *Similarity*

As in the $Sc \gg 1$ measurements in Part 1, the logarithmic forms of the dissipation rate fields in figures 2–5 suggest that the internal profile of scalar dissipation values across each of these layers appears to be at least roughly self-similar. The magnitude of the scalar dissipation clearly varies along the length of any given layer (and does so much more rapidly than for $Sc \gg 1$ in Part 1), yet the dissipation profiles across all of the layers in the present $Sc \approx 1$ data nevertheless appear at least qualitatively to have nearly the same internal structure. A detailed assessment of this internal structure in the dissipation layers is presented in §5, where comparisons with the self-similar canonical solutions for isolated strained laminar diffusion layers from Part 1 are also given.

3.5. *Thicknesses*

Finally, note that the thicknesses of the layer-like structures seen in figures 2–5 do not appear to span a very wide range. Although as noted above there is a greater variation in thickness among neighbouring layers than was the case at $Sc \gg 1$, the overall range of thicknesses appears qualitatively comparable to that seen in Part 1. A detailed analysis of the distribution of apparent diffusion layer thicknesses, including a correction based on isotropy that corrects for the layer orientations, will be given in §6, and an assessment of the scaling properties of the diffusion layer thickness distribution is given in §7.

4. Statistics of the scalar and dissipation rate fields

Data such as those in §3 allow various statistical measures of the $Sc \approx 1$ conserved scalar mixing process in turbulent flows to be determined and, by comparing with corresponding results from Part 1, allow identification of Schmidt number effects on these statistics. Moreover, the simultaneous conserved scalar and scalar dissipation rate fields obtained from these measurements allow determination of the joint distributions of scalar and scalar dissipation rates, which are of direct interest in many approaches to modelling turbulent reactive flows.

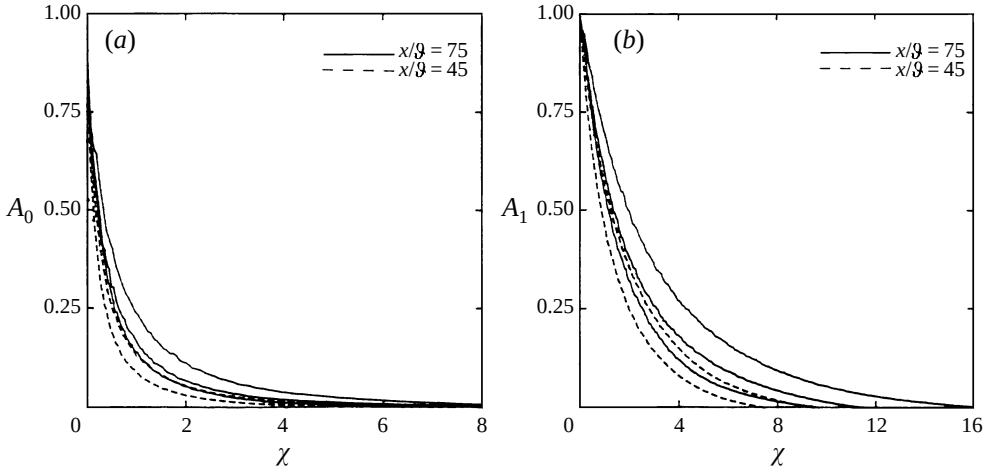

FIGURE 6. Results obtained at $x/\vartheta = 45$ and 75 for cumulative distributions (*a*) $A_0(\chi)$ and (*b*) $A_1(\chi)$ in (6.1) and (6.2) of Part 1 for $Sc \approx 1$ scalar mixing. Corresponding scaled distributions demonstrating similarity are shown in figure 7.

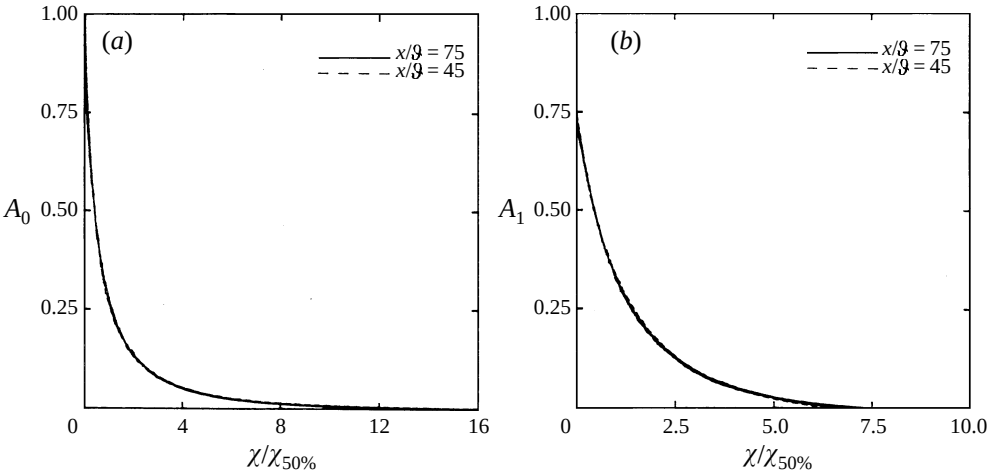

FIGURE 7. Cumulative distributions $A_0(\chi)$ and $A_1(\chi)$ from figure 6 scaled on measured local mean dissipation values $\chi_{50\%}$, showing self-similarity in scalar dissipation rates at $x/\vartheta = 45$ and 75.

4.1. *Cumulative distributions*

As was noted for the present $Sc \approx 1$ data in figures 2–5, as well as for the Sc 1 results in Part 1, high dissipation rates are seen in only a relatively small fraction of each of the measured data planes. This can be quantified by the cumulative distributions $A_0(\chi)$ and $A_1(\chi)$, defined in (6.1) of Part 1, for which results are shown in figure 6(*a*, *b*) for each of the five cases in table 1. The similarly of these distributions can be assessed by normalizing the result obtained for each case with the corresponding measured mean dissipation value $\chi_{50\%}$. These scaled distributions are shown in figure 7(*a*, *b*), where it can be seen that the different cases essentially collapse to a single and presumably quasi-universal curve in each panel, demonstrating that the scalar dissipation fields for all these cases are composed of similar distributions of dissipation rates. The cumulative distributions in figure 7(*a*, *b*) give a quantitative measure of the intermittent

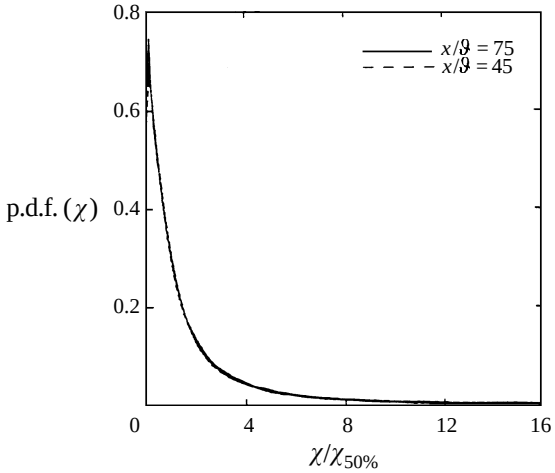

FIGURE 8. Probability densities p.d.f.(χ) of scalar dissipation rates measured at $x/\vartheta = 45$ and 75, scaled on local mean dissipation value $\chi_{50\%}$.

nature of the scalar dissipation fields, where the scalar dissipation rate is very low in most of the flow with only intermittent regions containing high dissipation rates. Moreover, the near-perfect collapse seen in figure 7 of these results obtained at these two different downstream locations, where the resolution is significantly different (see table 2), also indicates that the resolution achieved in these measurements at both locations is adequate to resolve essentially all of the structure in the scalar dissipation rate fields.

4.2. *Probability densities*

The self-similarity of the curves in figure 7 suggests that the associated probability densities of scalar dissipation rates will show a similar degree of universality. Accordingly, figure 8 shows the probability density for each of the five cases in table 1, with the dissipation values in each case scaled by their respective mean values. The self-similarity suggested by figure 7 is evident in the agreement obtained between all five curves. Note also that, as was seen in the $Sc \gg 1$ results in Part 1 and as is often assumed for dissipation p.d.f.s in turbulent flows, the resulting scalar dissipation distribution in figure 8 appears to be at least roughly lognormal. This will be examined in more detail in the results below.

In figure 9 we compare the scaled distribution obtained for $Sc \gg 1$ in Part 1 with the result for $Sc \approx 1$ from figure 8. It is apparent that both distributions are roughly similar, and both show high levels of intermittency. However it is also apparent that the $Sc \gg 1$ scalar dissipation fields showed somewhat stronger intermittency than do the present $Sc \approx 1$ fields, as evidenced by the corresponding distribution in figure 9 being more concave at low dissipation rates. This would appear consistent with the higher Péclet number ($Re\,Sc$) in the $Sc \gg 1$ fields, which have outer-scale Reynolds numbers of the order of 3000 but a Schmidt number of 2000, and therefore yield values much higher than the present $Sc \approx 1$ cases with outer-scale Reynolds numbers (and therefore Péclet numbers) of the order of 10000.

The dissipation values in figure 8 are obtained from two-component estimates of the true scalar gradient vector, and thus inherently underestimate the true dissipation values. As noted in Part 1, while it is impossible to obtain the true instantaneous local scalar dissipation rate at any point from such measurements spanning only two of the

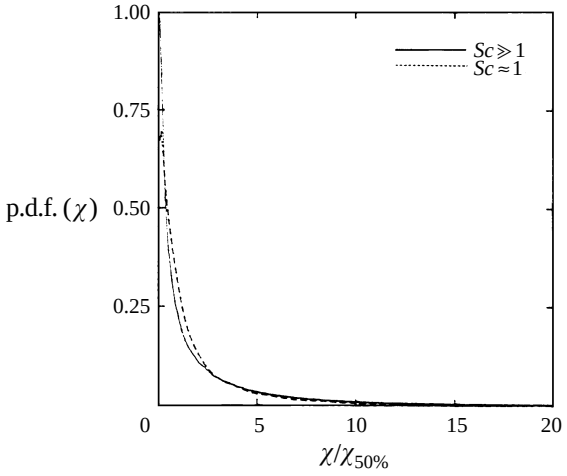

FIGURE 9. Comparison of p.d.f.(χ) obtained for Sc 1 in Part 1 and present results for $Sc \approx 1$.

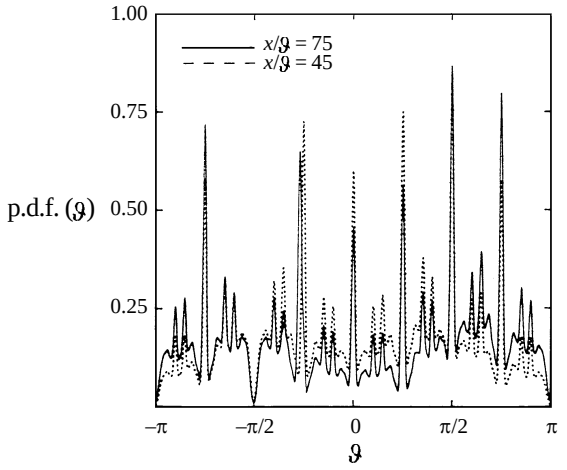

FIGURE 10. Distributions of in-plane scalar gradient vector orientations ϑ for two typical cases. Peaks result from differentiation of discrete data. Note slight tendency for preferred orientations along radial direction, corresponding to $\vartheta = \pm\pi/2$.

three spatial dimensions, it is nevertheless possible to obtain the *distribution* of true dissipation rates from such lower-dimensional measurements via a technique described by Dahm & Buch (1989) under the assumption of a known distribution of the scalar gradient vector orientations. If the scalar gradient orientations are assumed to be isotropically distributed, then the joint distribution $\beta(\vartheta,\ )$ of spherical orientation angles ϑ and as defined in Part 1 is simply $(1/4\pi)\sin$. The resulting projection of the true scalar gradient vector onto any measurement plane will then produce a uniform distribution $\beta(\vartheta)$ of apparent orientation angles in that plane. As a check on the validity of this isotropy assumption, the measured distributions of in-plane scalar gradient vector orientation angles ϑ at each of the two downstream locations are shown in figure 10. The spikes in these distributions, which occur at precisely regular intervals and with an extremely high degree of symmetry in their amplitudes, are due to the discrete nature of the data, as discussed in Part 1. Putting these spikes aside, the

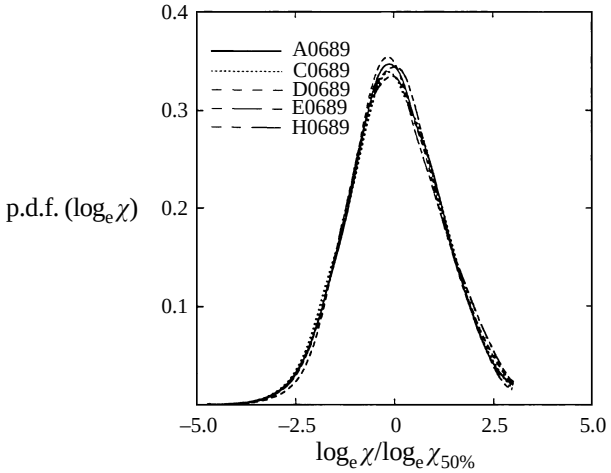

FIGURE 11. Distribution of the logarithm of the full three-dimensional scalar dissipation rates, obtained via isotropy as in the Appendix.

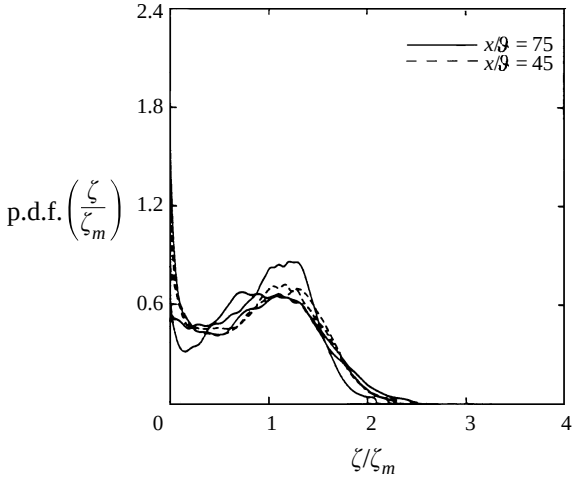

FIGURE 12. Distributions of conserved scalar values ζ scaled on measured local mean value ζ_m.

distributions obtained are indeed largely independent of ϑ, though a small and overall roughly sinusoidal variation with period π appears to be discernible. This would suggest a very slight degree of anisotropy corresponding to a tendency of the dissipation layers to lie along the downstream direction; that is, with their layer normals oriented in the radial direction, consistent with a similar observation in Part 1. This anisotropic tendency is somewhat more pronounced here than for the Sc 1 data, which is perhaps to be expected since the $Sc \approx 1$ measurements reach out beyond the local jet width while the Sc 1 measurements cover only a small region in the interior of the flow.

Accepting the assumption of isotropy in the scalar gradient field, the measured distributions of scalar dissipation rates in figure 8 can be converted to the corresponding distributions of three-dimensional scalar dissipation rates. The result is shown in figure 11 in logarithmic form, which corresponds to the distribution of values seen in the

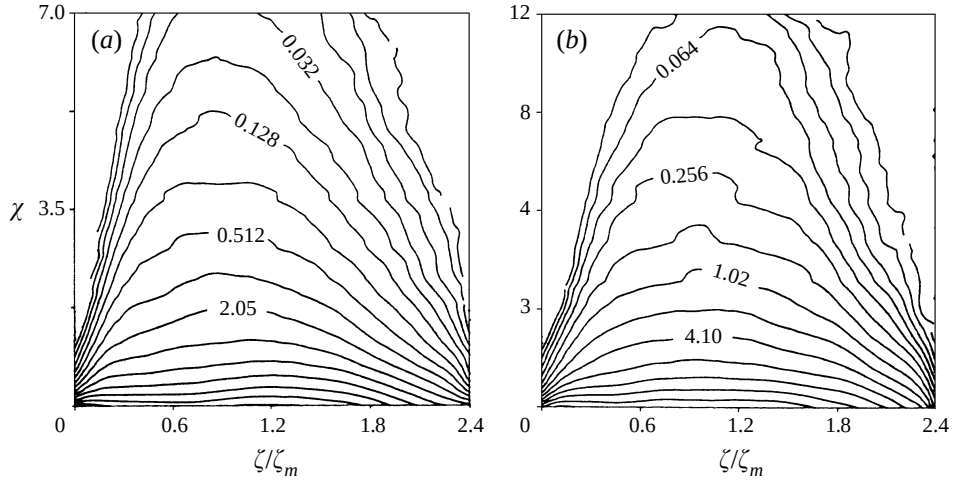

FIGURE 13. Joint probability densities of conserved scalar and two-dimensional scalar dissipation obtained at (*a*) $x/\vartheta = 45$ (D0689) and (*b*) 75 (A0689). Corresponding distributions for three-dimensional dissipation are shown in figure 14.

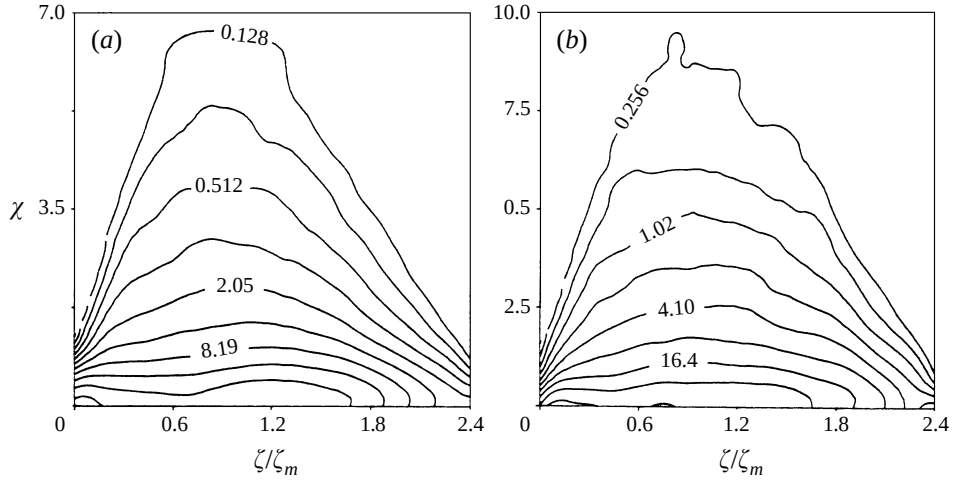

FIGURE 14. Joint probability densities of conserved scalar and three-dimensional scalar dissipation at (*a*) $x/\vartheta = 45$ and (*b*) 75, obtained from measured results in figure 13 via isotropy as in Appendix.

logarithmic maps in figure 2–5. Note that the result at very low dissipation values was obtained by linearly connecting the last non-zero dissipation value in the linear distributions in figure 8 to zero. A roughly lognormal form of the dissipation distribution is evident by the approximately Gaussian form of the result in figure 11. Note also that the agreement among these distributions, which were obtained at different levels of resolution (see table 2), further indicates that these measurements of the $Sc \approx 1$ scalar dissipation rate field are essentially fully resolved.

Figure 12 shows the distributions of conserved scalar values for each of the five cases in table 1, scaled by their respective mean values. Since the two x/ϑ values do not differ greatly, these distributions show relatively good agreement. In contrast to the corresponding result in Part 1, note that the peak scalar values for $Sc \approx 1$ are typically only about twice the mean value, whereas for Sc 1 the peak was found to be over four times the mean value.

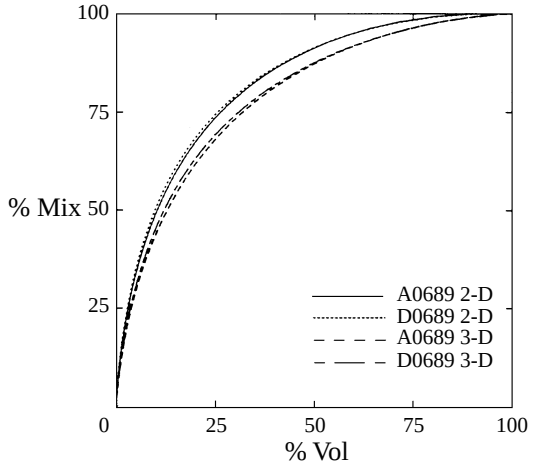

FIGURE 15. Cumulative distributions showing fractions of total mixing occurring in a given fraction of the volume, showing results at (*a*) $x/\vartheta = 45$ and (*b*) 75 from both two- and three-dimensional dissipation rates.

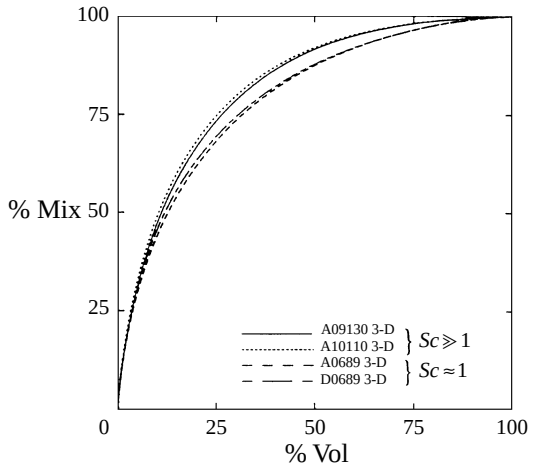

FIGURE 16. Comparison of cumulative distributions for mixing density in figure 15 from present $Sc \approx 1$ results and corresponding results for Sc 1 from Part 1. Results are shown for both two- and three-dimensional dissipation rates.

4.3. *Joint probability densities*

Figure 13(*a*, *b*) shows the measured joint distributions of the conserved scalar and scalar dissipation rate for the two axial locations. It is readily apparent from these results that $\zeta(\boldsymbol{x}, t)$ and $\chi(\boldsymbol{x}, t)$ are statistically independent, as is often assumed for modelling purposes. Note also that the contours shown increase logarithmically, with adjacent levels changing by factors of two. The dissipation values shown are the two-component estimates that result from differentiation within each data plane. Owing to the statistical independence between the conserved scalar and the scalar dissipation rate, the conditional two-dimensional scalar dissipation distributions obtained by integrating the results in figure 13 over narrow ranges of ζ can then be converted to the

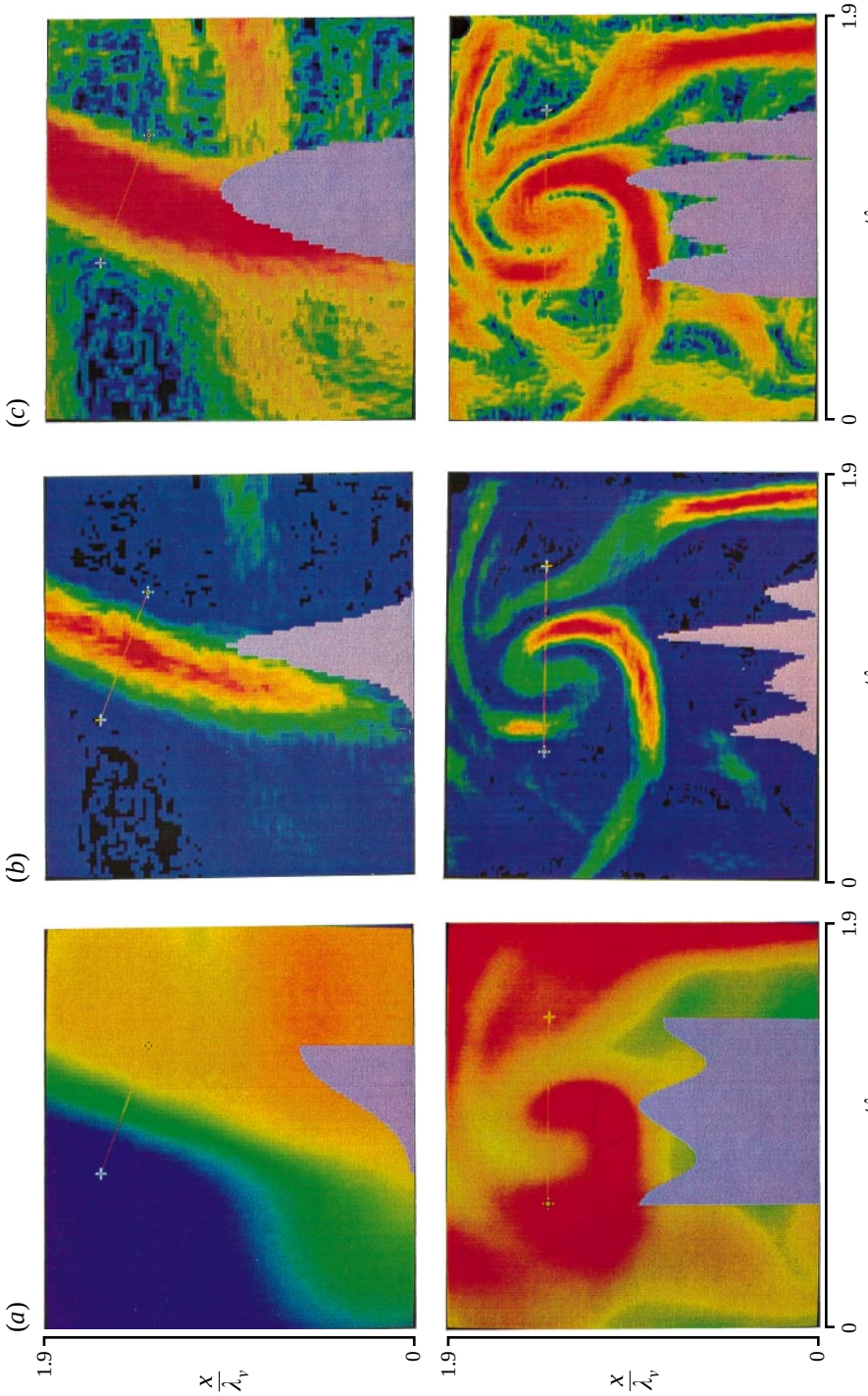

FIGURE 17. Typical layer-normal profiles through (*a*) the instantaneous conserved scalar, (*b*) scalar dissipation rate, and (*c*) logarithm of the scalar dissipation rate fields.

corresponding three-dimensional scalar dissipation distributions as in §4.2. These marginal distributions can then be recombined to produce the joint distribution of the conserved scalar and the three-dimensional scalar dissipation values. The result is shown in figure 14, where adjacent contours again differ by factors of two. These can be compared with the corresponding distributions for $Sc \gg 1$ scalar mixing in figure 23 of Part 1.

4.4. *Spatial density of the mixing process*

The cumulative distributions and probability densities described above verify the high level of internal intermittency characteristic of high-Reynolds-number turbulent mixing. This intermittency can be viewed more directly in terms of the fraction of the total flow volume required to achieve a given fraction of the total mixing. Figure 15 shows this result for each of the two axial locations, in each case showing the corresponding curves for the scalar dissipation rates obtained from both the two-component and three-component gradient vector distributions. The results for the full three-component scalar dissipation show that just 4% of the total flow volume accounts for 25% of the total mixing achieved, while 75% of the mixing is accomplished in 30% of the volume. Figure 16 compares these curves for $Sc \gg 1$ and $Sc \approx 1$ data, where it can be seen that in accordance with the results in §4.1 the $Sc \gg 1$ dissipation fields show slightly higher intermittency. The $Sc \approx 1$ scalar dissipation field requires about 30% of the total volume to achieve 75% of the total mixing, whereas in the large-Schmidt-number case this is accomplished in about 25% of the volume.

5. Internal structure of the dissipation layers

The extent to which the scalar dissipation layers in figures 2–5 conform to the simple local canonical solution for an isolated sheet-like scalar diffusion structure outlined in §7 of Part 1 can be determined by comparing the internal structure within the dissipation layers with this solution. In particular, the conserved scalar values across the dissipation layer would show an error function profile, while the scalar dissipation profile would be Gaussian and its logarithm would show an inverted parabolic form. These characteristic shapes can be compared with those in figure 17, where profiles along typical intersections through each of these fields are shown. Note that the profile shapes agree at least qualitatively with the corresponding functional forms noted above. While the $Sc \approx 1$ profiles appear to conform more closely to these canonical forms than do the corresponding $Sc \gg 1$ profiles in Part 1, it is likely that this is due to the higher spatial resolution relative to λ_D of the present measurements.

Quantitative comparisons with the canonical dissipation layer structure can be obtained using moments of the local scalar dissipation profiles, as was done for the $Sc \gg 1$ data in §7.4 of Part 1. In particular, the third moment can be characterized by the skewness S, which is zero for symmetric functions like the Gaussian form in (7.12) of Part 1. Similarly, the normalized fourth moment (the kurtosis K) for a full Gaussian profile is precisely 3, and if the Gaussian is clipped at its 20% points and renormalized becomes 2.26. Collecting values for S and K from all possible intersections through the dissipation layers in all the data planes allows the resulting distributions to be obtained. The statistics converge rather quickly. For example, figure 18 verifies that the measured skewness distribution converges after just a few planes, since each plane contributes a relatively large number of individual profile intersections. The resulting distributions of S and K at both downstream locations are shown in figure 19(a, b), where it can be seen

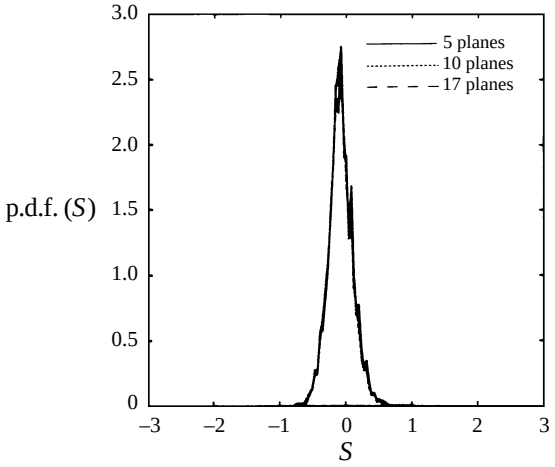

FIGURE 18. Distributions of skewness for all layer-normal profiles through isolated molecular diffusion layers in the $Sc \approx 1$ scalar dissipation rate fields, showing convergence with number of data planes analysed.

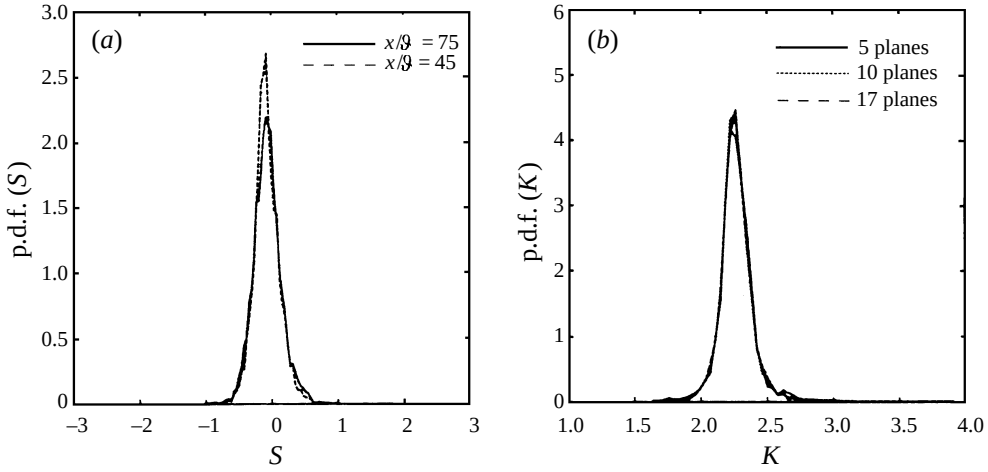

FIGURE 19. Distribution of (*a*) skewness and (*b*) kurtosis values for all layer-normal profiles at $x/\vartheta = 45$ (D0689) and 75 (A0689). Canonical solution in Part 1 gives $S = 0$ and $K = 2.25$.

that the skewness values are indeed narrowly distributed around zero, and the kurtosis values are distributed around 2.26, in good agreement with the canonical solution.

If the scalar dissipation rate fields were composed entirely of such isolated sheet-like strained laminar diffusion layers then, as noted in §7.4 of Part 1, the distribution of maximum dissipation values within each layer-normal profile, together with the distribution of scalar endpoint values ζ^+ and ζ^-, would completely define the probability density function of the scalar dissipation rate field. Equivalently, these endpoint values and the layer thickness determine the maximum dissipation value for each layer intersection as $\chi_{\max} \sim (\zeta^+ - \zeta^-)^2/\lambda_D^2$. Figure 20 shows the distribution of the local dissipation maxima from the $Sc \approx 1$ data, where good agreement is seen between the cases at $x/\vartheta = 45$ and 75 when scaled by their respective median values. In figure 21 this distribution is compared with the result obtained in Part 1 from the Sc 1

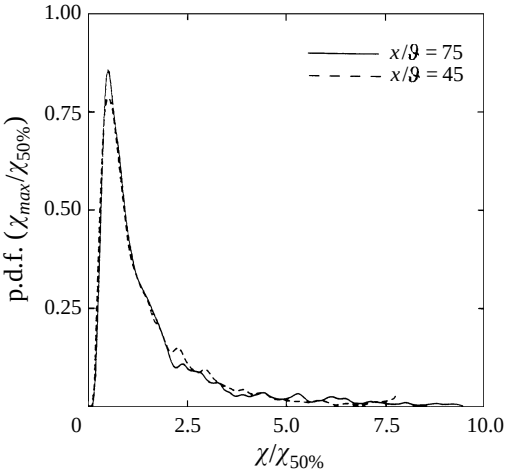

FIGURE 20. Distributions of layer-maximum dissipation values at $x/\vartheta = 45$ (D0689) and 75 (A0689).

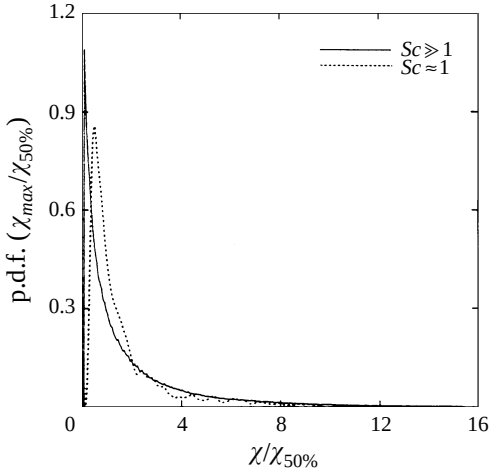

FIGURE 21. Comparison of layer-maximum dissipation values from present $Sc \approx 1$ results and corresponding results for $Sc \gg 1$ from Part 1.

measurements. The differences seen are conceptually consistent with the differences noted above in the levels of internal intermittency for the $Sc \approx 1$ and $Sc \gg 1$ dissipation rate fields.

6. Dissipation layer thicknesses

As was noted for both $Sc \gg 1$ and $Sc \approx 1$, the apparent thicknesses of the scalar dissipation layers in figures 7–13 of Part 1 and figures 2–5 above are seen to change from one case to another, but within the data from any one case the apparent thicknesses do not vary over a wide range. This is remarkable in view of the strain-diffusion analysis given in §7 of Part 1. In particular, from (7.6) of Part 1, when ϵ_{11} is of the order of the local inner-scale strain rate $(u/\delta)Re_\delta^{1/2}$, then the equilibrium strain-limited diffusion lengthscale would be $(\lambda/\delta) \sim Re_\delta^{-3/4}$ and corresponds to the local Kolmogorov scale. On the other hand, when ϵ_{11} is of the order of the local outer-scale

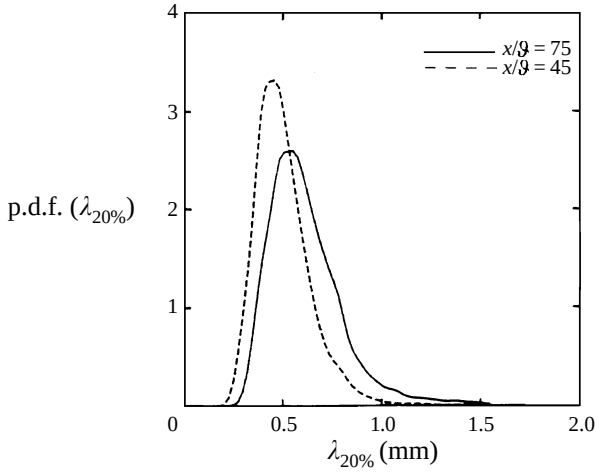

FIGURE 22. Distribution of measured in-plane scalar dissipation layer thicknesses at $x/\vartheta = 45$ (D0689) and 75 (A0689). Corresponding results corrected for orientation effects as in the Appendix are shown in figure 23.

strain rate (u/δ), then the resulting strain-limited equilibrium lengthscale becomes $(\lambda/\delta) \sim Re_\delta^{-1/2}$ and corresponds to the local Taylor scale. Since the strain rate field in turbulent flows is classically viewed as varying between these inner-scale and outer-scale limiting values, the resulting range of equilibrium lengthscales expected at even moderate values of the outer-scale Reynolds number Re_δ would be considerably larger than that seen in these figures.

Of course, some caution must be exercised in inferring the range of dissipation layer thicknesses from these figures, since the dissipation fields were obtained from the two-dimensional projection of $\boldsymbol{\nabla}\zeta(\boldsymbol{x}, t)$ onto the measurement plane. The out-of-plane component of the gradient vector was therefore not accounted for in the local dissipation value. As a consequence, if a layer-like structure were oriented largely tangent to the measurement plane, the two-dimensional dissipation obtained would appear to be very low, corresponding to blue values in the colouring schemes used. Since the yet lower dissipation rates corresponding to the tails of the normal profile across the layer would then be coloured lack, the apparent thickness of the layer might appear very similar to that of a layer oriented largely perpendicularly to the measurement plane.

To obtain an accurate assessment of the range of true dissipation layer thicknesses, a quantitative investigation to determine the distribution of layer thicknesses was undertaken involving a technique described in the Appendix that corrects for these orientation anomalies based on the assumption of isotropy in the scalar gradient field. This assessment was based entirely on the $Sc \approx 1$ data, since the higher relative spatial resolution allows a more accurate determination of the distribution of layer thicknesses. The local layer thickness $\lambda_{20\%}$ for each normal intersection through every dissipation layer was defined as the full width along the local layer-normal dissipation profile between the points where the dissipation had decreased to 20% of the local profile maximum value. Figure 22 shows the resulting apparent layer thickness distributions for the two axial locations in table 1. Note that there is a relatively narrow range of thicknesses at each downstream location. As might be expected from (4.1*b*) of Part 1, the measured thicknesses increase with increasing downstream location x/ϑ, owing

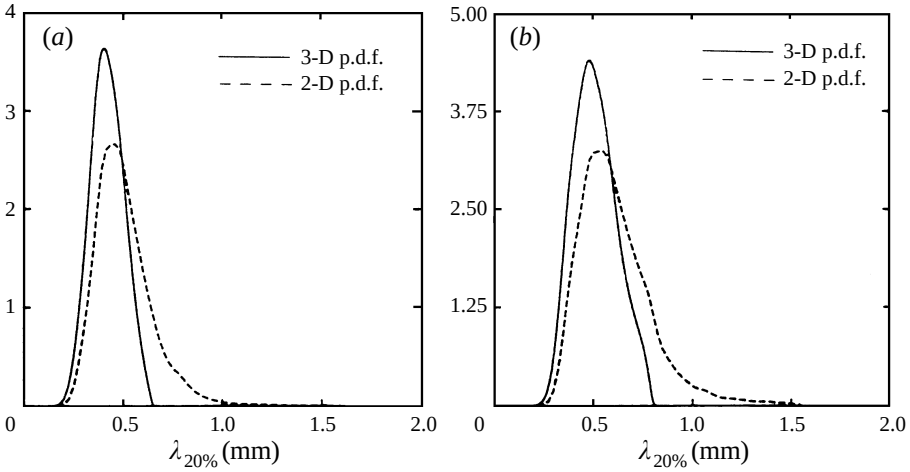

FIGURE 23. Distributions of apparent two-dimensional dissipation layer thicknesses (dashed line) and true three-dimensional layer thicknesses (solid line) at (*a*) $x/\vartheta = 45$ and (*b*) 75, obtained from results in figure 22 as described in the Appendix.

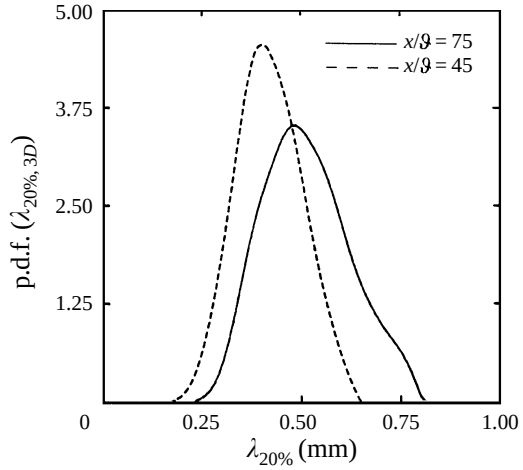

FIGURE 24. Comparison of true three-dimensional dissipation layer thicknesses at $x/\vartheta = 45$ and 75 from figure 23. Results scaled on local mean layer thickness are shown in figure 25.

both to the increase in δ and the decrease in Re_δ. Notice also that each of these distributions has a long tail extending to relatively large layer thicknesses, which corresponds to the contributions from layers intersecting the measurement plane at increasingly tangential orientations. An accurate determination of the true maximum and minimum layer thickness values requires that these orientation effects be removed from the distributions. In a similar manner as was done above and in Part 1 to statistically account for the missing scalar gradient vector component in the dissipation distributions, the Appendix presents the procedure for obtaining the distribution of true three-dimensional layer thicknesses from the measured distribution of apparent two-dimensional layer thicknesses under the assumption of isotropy in the $\boldsymbol{\nabla}\zeta(\boldsymbol{x}, t)$ field.

Figure 23 (*a*, *b*) shows the results obtained after applying this correction to each of

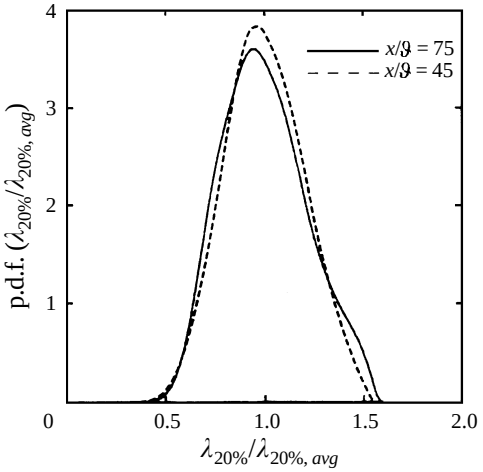

FIGURE 25. Distributions of true three-dimensional dissipation layer thicknesses at $x/\vartheta = 45$ and 75 from figure 24 scaled on local mean layer thickness, showing apparent similarity. Mean scalar dissipation layer thickness is $\lambda_D/\delta \approx 11.2 \cdot Re_\delta^{-3/4}\, Sc^{-1/2}$.

the apparent layer thickness distributions in figure 11. In particular, note that the tail at large thickness values in each of the original distributions disappears, while the smallest thickness values are essentially unchanged, since these should correspond to genuinely thin layers that intersect the measurement plane at nearly normal orientations. A comparison of the resulting three-dimensional layer thickness distributions at the two downstream locations is presented in figure 24, where the expected increase in layer thicknesses with increasing downstream location x/ϑ can be readily seen.

In figure 25 the three-dimensional layer thickness distributions from figure 24(a, b) are shown after each has been scaled with its mean thickness value. Note that the two scaled distributions in figure 25 collapse remarkably well, indicating a self-similar distribution of true three-dimensional dissipation layer thicknesses. Moreover, this collapse of the measurement results obtained at these two different downstream locations, having significantly different resolution (see table 2), further indicates that the present measurements are essentially fully resolved. Of particular importance for the purposes of this section is the observation in figure 25 that the largest layer thicknesses are roughly 1.5 times the local mean thickness value, and that the smallest layer thicknesses are approximately 0.5 times the local mean thickness. The total range of thicknesses thus spans only a factor of three.

The mean thickness values in figure 25 at $x/\vartheta = 45$ and 75 are 455 μm and 505 μm, respectively. From the conditions in table 1 and the scaling laws in (4.1a, b) of Part 1, the resulting constants in the thickness scaling $\lambda_{20\%}/\delta \equiv \Lambda\, Re_\delta^{-3/4}\, Sc^{-1/2}$ are found to be $\langle\Lambda\rangle = 14.9$ and 11.2 at $x/\vartheta = 45$ and 75, respectively. Taking the value at $x/\vartheta = 75$ to be more accurate owing to the somewhat higher relative resolution gives the corresponding range of scaling values

$$\langle\Lambda\rangle_{\max} \approx 16.8; \quad \langle\Lambda\rangle_{\text{mean}} \approx 11.2; \quad \langle\Lambda\rangle_{\min} \approx 5.6. \tag{7.1}$$

These characteristic values, and indeed the entire distributions in figure 25, would presumably be quasi-universal, and thus apply for sufficiently high outer-scale Reynolds numbers in all equilibrium turbulent shear flows.

7. Scaling of the dissipation layer thicknesses

The scalings constants in (7.1) assume that the entire range of diffusion layer thicknesses obey Kolmogorov scalings. However, if the maximum and minimum thicknesses scale differently with Reynolds number, then these scaling constants will appear to change as Re_δ changes. Accepting that the thinnest layers must follow Kolmogorov scaling, in view of the discussion in §6 perhaps the most plausible of such alternative Reynolds number dependencies is for the thinnest layers to be set by the local inner-scale strain rate $(u/\delta)\ Re_\delta^{1/2}$ and thus follow $Re_\delta^{-3/4}$ (Kolmogorov) scaling, and the thickest layers to be set by the local outer-scale strain rate (u/δ) and thus follow $Re_\delta^{-1/2}$ (Taylor) scaling.

To judge these two options from the layer thickness distributions in figure 25, it must be noted that the Re_δ range represented (see table 1) is too small to identify any Reynolds number effect that would result from a potential Taylor scaling of the thickest layers. However, if we accept that the thinnest layers *must* follow Kolmogorov scaling and postulate that the thickest layers follow Taylor scaling, then if all other factors in the two strain rate scalings are taken to be the same, this would require the *ratio* of the maximum to minimum thicknesses to be approximately $Re_\delta^{1/4}$. For the $Re_\delta \approx 10^4$ in each of the thickness distributions in figure 25, this would imply a ratio of the maximum to minimum thicknesses of about 10, while the measured ratio is only about 3. In view of the very high spatial resolution represented in these $Sc \approx 1$ measurements, it seems unlikely that the rather large difference in these ratios can be attributed to experimental uncertainty. On this basis, it is therefore tentatively concluded that both the maximum and minimum dissipation layer thicknesses follow Kolmogorov scaling, and that the Re_δ scalings inherent in (7.1) and the constants given are indeed correct.

8. Discussion and conclusions

The results presented here offer comparably detailed views of the fine-scale structure of $Sc \approx 1$ conserved scalar mixing in turbulent flows as did the results in Part 1 for $Sc \gg 1$ scalar fields. These imaging measurements have provided highly resolved data on the conserved scalar and scalar gradient fields, and give a physical picture of the fine-scale structure of the scalar mixing process. The excellent agreement of results obtained in figures 7(*a*, *b*), 8, 11, 12, 15, 19(*a*), 20 and 25 at two different downstream locations, with different levels of resolution as indicated in table 2, suggests that the resolution achieved in these measurements at both locations is adequate to resolve essentially all of the structure in the scalar energy dissipation rate fields.

Perhaps most noteworthy is the observation in §3 of a fundamentally sheet-like topology of the scalar dissipation rate field in $Sc \approx 1$ conserved scalar mixing, despite the fact that the lengthscale on which these layers are folded by vorticity gradients is comparable to the layer thickness. As was noted in Part 1, the topology of the scalar mixing process in turbulent flows is considerably simpler than that of the underlying vorticity field, since the dynamics of the former can sustain only sheet-like structures, whereas the latter can sustain both sheet-like and line-like structures (see §7 of Part 1). Moreover, the internal structure of these dissipation layers is the same as for $Sc \gg 1$ scalar mixing, and in good agreement with the canonical solution in §7.3 of Part 1. The present results have also determined the distribution of true dissipation layer thicknesses, which based on the above considerations should presumably apply to $Sc \gg 1$ scalar mixing as well. In particular, the thickness constant Λ for $\lambda/\delta \sim Re_\delta^{-3/4} Sc^{-1/2}$ ranges from 5.6 to 16.8, with the mean thickness corresponding to 11.2, where

the dissipation layer thickness λ and the local outer scale δ are defined as noted above and in Part 1. The distribution of thickness values appears to be self-similar and of the form given in figure 25, with the largest and smallest thicknesses tentatively appearing to both follow Kolmogorov ($Re_\delta^{-3/4}$) scaling.

Despite these similarities in the fine-scale structure of $Sc \gg 1$ and $Sc \approx 1$ conserved scalar mixing in turbulent flows, the present results have also shown a number of important differences. In particular, the orientations of neighbouring dissipation layers are nearly the same at $Sc \gg 1$, but at $Sc \approx 1$ can be very different. Indeed the patterns into which the present $Sc \approx 1$ dissipation layers are arranged by the continual stretching and folding of the underlying strain rate and vorticity fields bears little resemblance to those seen at $Sc \gg 1$ in Part 1. Also, the peak conserved scalar value relative to the local mean seen in these $Sc \approx 1$ data in figure 12 is considerably lower than that found in figure 22 of Part 1. The difference is presumably a consequence of the higher relative diffusivity in the present case.

As was noted in §7 of Part 1, the sheet-like fine-scale structure of scalar energy dissipation rate fields in turbulent flows, both at $Sc \gg 1$ and $Sc \approx 1$, is a result solely of the strain-diffusion dynamics at diffusive scales of the flow. As a consequence, the existence of this canonical fine-scale structure does not depend on either the Reynolds number or the downstream location in the flow. The present results, obtained at 39 and 65 diameters downstream of the nozzle exit, showed the same structure when scaled on appropriate variables. Indeed, the sheet-like structures are not a remnant of the boundary conditions at the nozzle exit, but rather are continually created by the competition between the thinning action of the local strain rate field and the thickening that results from molecular diffusion. The only effect of changing either Re_δ or the local outer scale $\delta(x)$ is a change in the thickness of the sheet-like structures in accord with $\lambda/\delta \sim Re_\delta^{-3/4}\, Sc^{-1/2}$, and an equal change in the lengthscale on which they are folded by gradients in the vorticity field. The ratio of these two scales, however, depends only on Sc, and thus no fundamental change in the fine-scale structure results except by changing the Schmidt number.

The present observation of a fundamentally layer-like topology in the fine-scale structure of $Sc \approx 1$ conserved scalar mixing in turbulent shear flows has considerable implications for modelling of non-equilibrium mixing-chemistry coupling in non-premixed or partially premixed turbulent combustion processes. In that case, the scalar quantity of interest is the local mass fraction of atoms originating in, say, the fuel stream. Despite the fact that molecular species in the fuel and oxidizer streams are not conserved under the ensuing chemical reactions, elemental mass fractions are conserved and can be rigorously related to the local instantaneous values of the elemental composition ζ and mixing rate χ. The former determines the local adiabatic equilibrium composition of molecular species that form from the elemental pool, and the latter allows for non-equilibrium corrections to this composition. A broad class of approaches collectively termed 'flamelet models' aims to relate the local conserved scalar value and scalar dissipation rate to the local molecular mass fractions, and thus plays a key role in turbulent combustion theory and in practical approaches to reducing emissions of regulated trace species from turbulent combustion processes. The results from the present study, and in particular the observation that essentially all the molecular mixing occurs in strained laminar sheet-like diffusion layers with an internal structure that agrees with the canonical solution in §7 of Part 1, provide a rigorous starting point for such flamelet models. The implications of this for mixing-chemistry coupling in turbulent combustion will be examined in detail in the forthcoming Part 3.

The Rayleigh scattering experiments were performed with Robert W. Dibble, Marshall B. Long, Dominique C. Fourguette and Robert S. Barlow at the Combustion Research Facility of Sandia National Laboratories (Livermore, CA), which is supported by the Department of Energy, Office of Basic Energy Sciences, Division of Chemical Science. Various parts of the work described were supported by the Air Force Office of Scientific Research (AFOSR) under Grant No. 89-0541 and Grant No. F49620-95-1-0115, by the Gas Research Institute (GRI) under Contract Nos. 5087-260-1443 and 5088-260-1692, and with discretionary funds provided by the University of Michigan.

Appendix. Deconvolution of the two-dimensional layer thickness distribution to the three-dimensional distribution

The two-dimensional scalar dissipation rate fields consist of scalar gradient layers with nearly isotropic orientations. Since the measurement plane is fixed, it will intersect the layers at random orientations, and therefore the apparent thickness of the layers differs from their true thickness. Correcting any apparent layer thickness to its true thickness requires knowing its orientation angle. Under the assumption of isotropic orientations, the distribution of dissipation layer thicknesses $\beta(\lambda)$ can be determined from the measured distribution of apparent two-dimensional thickness in a manner analogous to that outlined in Dahm & Buch (1989) for the distribution of scalar dissipation rates.

Consider measurements of the layer thickness in directions oriented at some angle ϑ to the layer normal. The true thickness is then related to its apparent thickness in the measurement plane by

$$\lambda = \lambda_{app} \sin\phi. \tag{A 1}$$

The cumulative distribution function, $B(\lambda_{app};\lambda)$, gives the probability that any such two-dimensional estimate, λ^*_{app}, of λ will fall below the threshold value λ_{app} and is expressed by the probability $P(\quad < \phi^* < \pi - \vartheta)$. This probability is equivalent to

$$P(\quad < \quad < \pi - \quad) = \int_{-\pi}^{\pi} \int_{-\pi}^{\pi -} \beta(\ ',\ ')\, \mathrm{d}\ '\, \mathrm{d}\ ', \tag{A 2}$$

Where $\beta(\ ,\vartheta)$ is the joint distribution of orientation angles. If the scalar gradient vector orientations are isotropic, then all orientations of the layer normal and the measurement plane are equally probable, so

$$\beta(\ ,\vartheta) = (1/4\pi \sin\ , \tag{A 4}$$

giving

$$B(\lambda_{app}/\lambda) = [1-(\lambda_{app}/\lambda)^{-2}]^{1/2}. \tag{A 5}$$

Equation (A 5) then gives the resulting layer thickness distribution if all the layers were the same thickness and oriented isotropically. Even if the scalar field were not isotropic, (A 5) could still be formulated, provided the anisotropy could be characterized in terms of $\beta(\ ,\vartheta)$ to obtain an analogous result. From the cumulative distribution in (A 5), the probability density for λ_{app}/λ can then be obtained as

$$\beta(\lambda_{app}/\lambda) = \frac{(\lambda_{app}/\lambda)^{-3}}{[1-(\lambda_{app}/\lambda)^{-2}]^{1/2}}. \tag{A 6}$$

This gives the distribution of measured, apparent layer thicknesses λ_{app} if all the true layer thicknesses were equal to λ and were isotropically oriented.

Now consider all remaining occurrences of the scalar gradient and similarly group these into narrow intervals centred at $\lambda_1, \ldots, \lambda_i, \ldots, \lambda_N$, namely,

$$\beta(\lambda) = \sum_{i=1}^{N} a_i \, \delta(\lambda), \tag{A 7}$$

where each of the weights, a_i, gives the fraction of the time that λ lies in the ith interval. Since the functions $\beta(\lambda_{app}/\lambda_i)$, $i = 1, \ldots, N$, form an independent (though non-orthogonal) basis set under the physically correct constraint that all the a_i must be non-negative, the p.d.f. $\beta(\lambda_{app})$ obtained from the two-dimensional estimates for the scalar dissipation is then a linear combination of the elementary p.d.f.s $\beta(\lambda_{app}/\lambda_i)$, namely

$$\beta(\lambda_{app}) = \sum_{i=1}^{N} a_i \beta(\lambda_{app}/\lambda_i), \tag{A 8}$$

with suitable renormalization to unity area. The weights, a_i, can then be determined from $\beta(\lambda_{app})$ by decomposing the p.d.f. into this basis set as

$$a_i = \frac{\displaystyle\int_{\lambda_{i,app}}^{\lambda_{i+1,app}} \left[\beta(\lambda_{app}) - \sum_{j=1}^{i-1} a_j \beta(\lambda_{app}/\lambda_j) \right] \mathrm{d}\lambda_{app}}{\displaystyle\int_{\lambda_{i,app}}^{\lambda_{i+1,app}} \beta(\lambda_{app}/\lambda) \, \mathrm{d}\lambda_{app}}, \tag{A 9}$$

and the true scalar dissipation p.d.f. $\beta(\lambda)$ is reconstructed from the weights a_i using (A 7). The reconstruction proceeds from the lowest apparent thickness value, since any given layer can only appear thicker in the measurement plane. Each narrow range of layer thicknesses therefore only contributes to the distribution at greater thicknesses.

REFERENCES

Buch, K. A. & Dahm, W. J. A. 1996 Experimental study of the fine scale structure of conserved scalar mixing in turbulent shear flows. Part 1. *Sc* 1. *J. Fluid Mech.* **317**, 21–71.

Dahm, W. J. A. & Buch, K. A. 1989 Lognormality of the scalar dissipation pdf in turbulent flows. *Phys. Fluids* A **1**, 1290–1293.

Papanicolaou, P. N. & List, E. J. 1988 Investigations of round vertical turbulent buoyant jets. *J. Fluid Mech.* **195**, 341–391.